

Interaction of hot spots and terahertz waves in $\text{Bi}_2\text{Sr}_2\text{CaCu}_2\text{O}_8$ intrinsic Josephson junction stacks of various geometry

S. Guénon,¹ M. Grünzweig,¹ B. Gross,¹ J. Yuan,² Z. G. Jiang,³ Y. Y. Zhong,³ M. Y. Li,³ A. Iishi,² P. H. Wu,³ T. Hatano,² R. G. Mints,⁴ E. Goldobin,¹ D. Koelle,¹ H. B. Wang,^{2,*} and R. Kleiner^{1,†}

¹*Physikalisches Institut, Experimentalphysik II and Center for Collective Quantum Phenomena, Universität Tübingen, Auf der Morgenstelle 14, D-72076 Tübingen, Germany*

²*National Institute for Materials Science, Tsukuba 3050047, Japan*

³*Research Institute of Superconductor Electronics, Nanjing University, Nanjing 210093, China*

⁴*The Raymond and Beverly Sackler School of Physics and Astronomy, Tel Aviv University, Tel Aviv 69978, Israel*
(Received 7 May 2010; revised manuscript received 16 September 2010; published 6 December 2010)

At high enough input power in stacks of $\text{Bi}_2\text{Sr}_2\text{CaCu}_2\text{O}_8$ intrinsic Josephson junctions a hot spot (a region heated to above the superconducting transition temperature) coexists with regions being still in the superconducting state. In the “cold” regions cavity resonances can occur, synchronizing the ac Josephson currents and giving rise to strong and stable coherent terahertz (THz) emission. We investigate the interplay of hot spots and standing electromagnetic waves by low-temperature scanning laser microscopy and THz emission measurements, using stacks of various geometries. Standing electromagnetic wave patterns and THz emission are observed for a disk-shaped sample. The growth of a hot spot with increasing input power is monitored by small detector junctions surrounding a large rectangular mesa. For two rectangular mesas equipped with two current injectors and one arrow-shaped structure we show that the standing wave can be turned on and off in various regions of the stack structure, depending on the hot-spot position. The results support the picture of the hot spot acting as a reflective termination of the cavity, formed by the cold part of the mesa.

DOI: [10.1103/PhysRevB.82.214506](https://doi.org/10.1103/PhysRevB.82.214506)

PACS number(s): 74.50.+r, 74.72.-h, 85.25.Cp

I. INTRODUCTION

Josephson junctions are attractive for the generation of high-frequency electromagnetic radiation because the frequency of emission is tunable by the voltage across the device. A Nb-based Josephson flux flow device was used as a local oscillator in a highly optimized integrated superconducting receiver operating up to about 600 GHz.¹ In the oscillator a row of Josephson fluxons is created by applying a magnetic field parallel to the junction barrier. The fluxons move along the barrier layer exciting junction cavity resonances. The emission frequency corresponds to the cavity resonance frequency and is tunable by choosing different resonances. In this on-chip design the Josephson oscillator delivers a power of a few microwatt to a superconducting mixer. However, the *off-chip* output power obtained from more typical junctions is only in the nanowatt range. Thus, to obtain a reasonable power output, arrays of many junctions should be synchronized.^{2–7} While Nb-based junctions are limited by the superconducting energy gap to frequencies below 1 THz, intrinsic Josephson junctions (IJJs) (Refs. 8–10) in $\text{Bi}_2\text{Sr}_2\text{CaCu}_2\text{O}_8$ (BSCCO) are, at least in principle, able to operate up to several terahertz (THz). Stacks of many junctions can be made, e.g., by patterning mesa structures on top of single crystals. For many years, investigations focused on small structures consisting of some 10 IJJs with lateral sizes of a few micron.^{11–23} Here, the IJJs in the stack most often tended to oscillate out of phase or were not synchronized at all.

Recently, coherent off-chip THz radiation with an extrapolated output power of some microwatt was observed from stacks of more than 600 IJJs with lateral dimensions in the 100 μm range.²⁴ Phase synchronization involved a cav-

ity resonance oscillating along the short side of the mesa. In contrast to many previous experiments no external magnetic field was applied to create Josephson fluxons. This finding triggered numerous experimental^{25–36} and theoretical studies,^{5,37–50} the latter being based on either Josephson vortex-type or plasmonic excitations, coupled to cavity modes,^{5,37–46,49,50} on synchronization via shunting networks^{48,51,52} or on nonequilibrium effects caused by quasiparticle injection.⁴⁷

Many of the experimental results were obtained at relatively low-bias currents through the mesa and moderate dc power input (<1 mW).^{24–28,34–36} Under such conditions there is no severe self-heating of the mesa, and the THz emission observed presumably can be described by more or less standard Josephson physics and electrodynamics. On the other hand, one also observes strong THz emission at high input power, where self-heating is severe.^{32,33} Basically all junctions in the stack oscillate coherently also in this high-bias regime, which has the advantage of allowing a stable and reproducible bias. By contrast, at low bias some of the junctions in the mesa can switch between the resistive state and the zero voltage state, causing multibranch hysteric current-voltage characteristics.

For 330- μm -long rectangular mesa structures of widths between 30 and 80 μm low-temperature scanning laser microscopy (LTSLM) revealed that in the high-bias regime a hot spot,^{53,54} i.e., a region heated to above the critical temperature T_c , forms.^{31,32} It effectively separates the stack into a “cold” region, which is superconducting, and a hot part, which is in the normal state. The temperature of the cold part was estimated to be of order 50–70 K.^{31,32,51} At certain values of bias current, where also the THz emission is strongest, the hot spot is accompanied by standing-wave patterns. One

TABLE I. Parameters of the samples investigated: shape, in-plane dimensions, thickness, critical temperature, transition width, and annealing conditions. Sample 2 in addition was surrounded by 10 μm wide, quadratic mesa structures consisting of 15–20 IJJs.

Sample	Shape	In-plane dimensions	Thickness (μm)	T_c (K)	ΔT_c (K)	Annealing conditions
1	Disk	200 μm diameter	0.9	86.6	1.5	600 °C, vacuum, 65 h
2	Rectangular	330 \times 70 μm^2	0.5	87.6	1.5	600 °C, vacuum, 72 h
3	Rectangular	330 \times 80 μm^2	1	83	1.5	600 °C, 1 atm, 99% Ar, 1% O ₂ , 48 h
4	Rectangular	330 \times 70 μm^2	0.8	86.8	1.1	600 °C, 1 atm, 99% Ar, 1% O ₂ , 48 h
5	Arrow	Subsections 300 \times 50 μm^2	1	87.6	1.5	600 °C, vacuum, 72 h

thus faces THz generation in a highly nonequilibrium situation. The underlying physics may differ from the low-bias case, requiring detailed investigation.

In the low-bias case the emission frequency is essentially fixed by the mesa geometry. By contrast, in the high-bias regime it can be varied by up to 40% by changing the bias current and the bath temperature.³² The variation matches the Josephson-frequency voltage relation, showing that Josephson currents are at least a major source of the emission observed. Two factors contribute to the tunability at given bath temperature. First, it was found that, when increasing the bias current, the mode velocity of the cavity resonance decreases.³¹ Second, the size of the hot spot grows with increasing bias current and, correspondingly, the size of the cold part of the mesa shrinks. Assuming that electromagnetic waves are reflected at the hot-spot boundary one faces a cavity with variable size and mode velocity and thus variable resonance frequency. Unfortunately, in the experiments reported in Refs. 31 and 32 these two factors were varied by only one quantity, namely, the bias current injected into the mesa.

In this paper we present a study of mesa structures of different geometry, in order to provide more information on hot-spot and wave formation and to examine possibilities to manipulate both hot spot and waves in a controlled way. For a rectangular mesa the standing-wave patterns visible in LTSLM basically consist of a sequence of straight stripes. It is hard to decide whether the electric or the magnetic part of the cavity mode is imaged. One might even argue that the stripes do not originate from an electromagnetic cavity mode. By contrast, a cylindrical mesa produces nontrivial resonance patterns.⁴¹ In Sec. III A we will show LTSLM and THz emission data for such a structure. As we will see, the pattern observed is fully compatible with an electromagnetic standing wave. The data indicate that the magnetic part of the cavity mode is imaged. Regarding hot-spot formation, the case of the BSCCO mesa structures is quite different from the “standard case” in thin-film bridges, where one observes hot spots as an interplay between the zero-voltage superconducting state below T_c and the resistive state above T_c .^{53,54} Here, typically, current flow is along a thin-film layer. In our case we have to consider a stack of tunnel junctions biased in their *resistive state* also below T_c . For conventional superconducting tunnel junctions, instead of hot-spot formation, the appearance of superconducting regions with suppressed energy gap upon strong current injection has been discussed.^{55–59} One should thus address this scenario as an

alternative, i.e., one should consider the case where the “hot-spot” area observed in LTSLM is still superconducting. In Sec. III B we will discuss data for a rectangular mesa which is surrounded by small detector mesas. The critical currents of these detector mesas approach zero when the front of the hot spot passes by. This is consistent with the hot-spot interpretation but hard to explain in the suppressed gap state scenario. We then turn to rectangular mesa structures that were contacted by two current injection points (Sec. III C). This configuration allowed to change the hot-spot position and to switch on and off standing-wave patterns in different sections of the mesa at nearly constant input power. The results support the picture of a variable-size cavity adjusted by the hot-spot position. Finally, in Sec. III D we will show data for an arrow-shaped mesa. Although equipped with only one current injector the geometry allowed to independently excite standing waves in various segments of the arrow, further confirming the picture of variable-size cavities terminated by the hot spot.

The paper is organized as follows. In Sec. II samples are characterized and the measurement techniques are described. Data for the different mesa structures are presented in Sec. III. Conclusions are given in Sec. IV.

II. SAMPLE PREPARATION AND MEASUREMENT TECHNIQUES

For the experiments BSCCO single crystals were grown by the floating zone technique in a four lamp arc-imaging furnace. Annealing conditions and the superconducting transition temperatures of the crystals used are listed in Table I. To provide good electrical contact the single crystals were cleaved in vacuum and a 30 nm Au layer was evaporated. Then, conventional photolithography and Ar ion milling was used to prepare mesas of various shapes and thicknesses. Insulating polyimide was used to surround the mesa edges at which Au wires were attached to the mesa by silver paste. Other Au wires were connected to the big single-crystal pedestal as grounds. Note that, since the large base crystals are not atomically flat, the foot of the mesa and the ground will, in general, be located in different CuO₂ layers. Consequently there can be a few additional IJJs of large size but not well-defined properties; partially, these layers are etched during ion milling, partially, they are shunted by the Au layer. While the parasitic IJJs contribute only marginally to the current-voltage characteristics (IVCs) of the mesas they can, at suf-

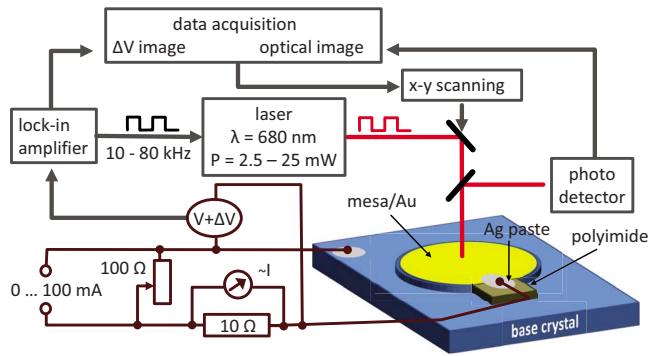


FIG. 1. (Color online) The LTSLM imaging system together with a sketch of a disk-shaped mesa.

ficiently high bias, strongly contribute to the LTSLM signal. Examples will be given.

Below we discuss results from five samples, cf. Table I. Sample 1 was disk shaped with a diameter of $200\ \mu\text{m}$ and a thickness of $0.9\ \mu\text{m}$, corresponding to a stack of 600 IJJs. The mesa was contacted near its outer edge, as sketched in Fig. 1. The $330 \times 70\ \mu\text{m}^2$ large and $0.5\text{-}\mu\text{m}$ -thick rectangular sample 2 was contacted on the right edge, cf. inset in Fig. 6(a). It was surrounded by much smaller, $10\text{-}\mu\text{m}$ -wide, square-shaped mesa structures consisting of 15–20 IJJs. To fabricate the detector mesas a U-shaped “mesa” was etched together with the main mesa. This structure surrounds the main mesa and is visible as a dark stripe in the inset of Fig. 6(a). Further etching of this structure yielded the small mesa structures. Subsequently the small mesas and the main mesa were contacted with a Au layer. The distance of the small mesas (used for thermometry) to the main mesa was $10\ \mu\text{m}$. The rectangular samples 3 and 4 were $330\ \mu\text{m}$ long, $1\ \mu\text{m}$ thick and, respectively, $80\ \mu\text{m}$ and $70\ \mu\text{m}$ wide. They were contacted at two edges, cf. Figs. 7(a) and 8(a). The arrow-shaped sample 5, cf. Fig. 9, consisted of three $330\ \mu\text{m}$ long and $50\ \mu\text{m}$ wide rectangular subsections rotated by 60° relative to each other and connected at one end (the top of the arrow). The mesa thickness was $1\ \mu\text{m}$. It was contacted at the end of the main stem of the arrow.

In order to provide a load line for stable operation, the mesas were biased using a current source and variable resistor in parallel to the mesa, see Fig. 1. The voltage measured across the mesa includes the resistance of the contacting Au wires and the resistance between these wires and the mesa. In the data discussed below this resistance (typically around $5\ \Omega$) is subtracted.

LTSLM measurements were performed in Tübingen. For sample 1 additional THz emission measurements were performed in Tsukuba. The LTSLM setup is shown schematically in Fig. 1. The beam of a 25 mW laser diode (wavelength 680 nm) is modulated at frequencies between 10 and 80 kHz, deflected by a scanning unit and focused onto the sample surface. The incoming laser power was typically attenuated by a factor of 10 using optical attenuators. Furthermore, the gold layer covering the mesa surface reflects at least 90% of the laser light, resulting in an absorbed CW laser power of order $100\ \mu\text{W}$. The laser spot size is $1\text{--}2\ \mu\text{m}$. Simulations, performed using COMSOL simulation

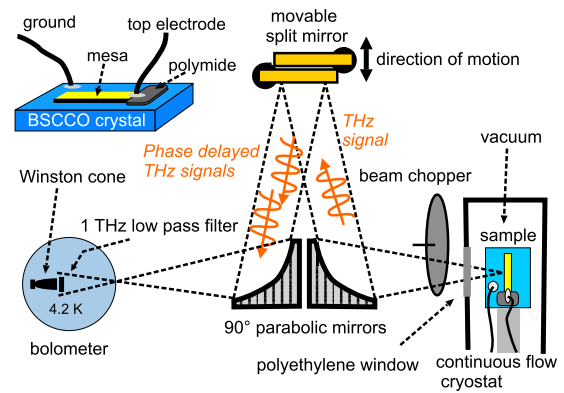


FIG. 2. (Color online) Schematic of the THz emission setup together with a sketch of a rectangular mesa contacted on its right edge.

software, revealed that the laser spot locally heats by 2–3 K an area of a few square micron and about $0.5\ \mu\text{m}$ in depth.³¹ In this area both the in-plane and out-of-plane critical supercurrent densities and resistivities change, causing a global change $\Delta V(x,y)$ in the voltage V across the mesa. Here, x and y denote the in-plane position of the laser spot. $\Delta V(x,y)$ is detected using lock-in techniques and serves as the contrast for the LTSLM image. Below, when quoting ΔV , for simplicity we will omit the coordinates (x,y) . Using the reflected laser light also optical images can be generated.

In general, an LTSLM image of a mesa will show some background signal arising, e.g., from the overall reduction in the c axis resistivity with increasing temperature. On top of that standing waves can be imaged due to the beam-induced local change in the quality factor, leading to a strong signal ΔV at antinodes and a weak signal at nodes. One observes the time-averaged intensity of either the electric or the magnetic field component. Which component dominates may depend on both the bias and the bath temperature. For Nb tunnel junctions the response was shown to primarily arise from the magnetic field component.⁶⁰ For IJJ stacks the situation is less clear; however, below we will show an example (sample 1) where the LTSLM response was most likely due to the magnetic field. Regarding the hot spot there is a strong signal ΔV when the laser beam illuminates its edge, i.e., the superconducting/normal boundary.^{31,61} By contrast, ΔV is small in the interior of the hot spot and in the cold part of the mesa. A typical signature of the hot spot is that its size grows with increasing dc power IV dissipated in the sample. Here, I denotes the dc current through the mesa. For wide mesas having widths of $70\ \mu\text{m}$ or more, the hot spot is circular and, when its diameter is large enough, is seen as a ring-shaped structure.³¹ For narrower mesas the hot spot often is “one dimensional,” i.e., its boundaries form straight lines parallel to the short side of the mesa.^{31,32} Below, examples for both cases will be shown.

The THz emission setup is shown schematically in Fig. 2 together with a sketch of a rectangular mesa. The interferometer is similar to the one in Ref. 62 with the difference that in our case a bolometer is used as a detector. The crystal is mounted in vacuum on the cold finger of a continuous flow He cryostat. A polyethylene window is used which is trans-

parent at the frequencies of interest. The emitted radiation, chopped with a frequency of 13 Hz, is collected by a 90° off-axis parabolic mirror (2" diameter, focal length 100 mm) and deflected toward two lamellar split mirrors dividing the incoming radiation into two beams with almost the same intensity. A phase difference is introduced by moving one of these mirrors with a translation stage. Via a second parabolic mirror the radiation is deflected to the bolometer. A 1 THz low-pass filter is used in front of the Winston cone. This setup can be used in two modes. In the first mode the emitted power of the mesa is recorded for different bias currents. The mirror is in the neutral position (i.e., no phase difference is introduced) for this purpose. In the second mode the auto-correlation function (emitted power vs mirror position) is acquired, which is mapped into a spectrum using fast Fourier transformation. The numbers we quote below are based on the *detected* power, ignoring additional losses (by a factor of 2–5) from the continuous flow cryostat window and the mirrors. The solid angle of our setup, defined by the aperture of the Winston cone in front of the bolometer, is 0.04 sr. The frequency resolution, depending on the maximum mirror displacement, is 10–15 GHz.

III. RESULTS

A. Standing waves, hot-spot formation, and THz emission in a disk-shaped mesa

We first discuss data of disk-shaped sample 1 which had a radius a of 100 μm . Disk-shaped mesa structures have been analyzed theoretically and considered promising for THz emission in Ref. 41. THz emission from such a structure is reported in Ref. 35. In our context we are, on one hand, interested in imaging the corresponding wave patterns. On the other hand the question arises whether or not hot-spot formation is supporting cavity modes in this geometry.

In the disks, the c axis electric field component is given by the time derivative of a term \tilde{P} describing Josephson plasma oscillations at frequency ω and having the form $\tilde{P}(r, t) = A g_{mn}(r) \sin(\omega t + \varphi)$ with some amplitude A and some initial phase φ . In cylindrical coordinates (ρ, ϕ) the function $g_{mn}(r) = J_m(\chi_{mn}^c \rho/a) \cos(m\phi)$, where χ_{mn}^c is the n th zero of the first derivative of Bessel function J_m . The in-plane magnetic field is proportional to the curl of $\tilde{P} \cdot e_z$ with the out-of-plane unit vector e_z . The resonance frequency is given by $c' \chi_{mn}^c / 2\pi a$ with the mode velocity c' .

Figure 3(a) shows by blue dots connected by a solid line the IVC of sample 1, as measured during LTSLM at $T = 19$ K (the IVC shown by green dots connected by a dotted line will be discussed below in the context of THz emission measurements). For bias currents between 22 and 25 mA there are instabilities on the resistive branch indicative of hot-spot formation.³¹ In addition, some of the junctions may switch between the resistive state and the zero voltage state. Indeed one can trace out several different branches in this region by sweeping the bias current back and forth. Figures 3(b)–3(f) show LTSLM images taken at different bias points. The bias lead, attached on the left side of the disk, as sketched in the inset of Fig. 3(a), is visible in all LTSLM

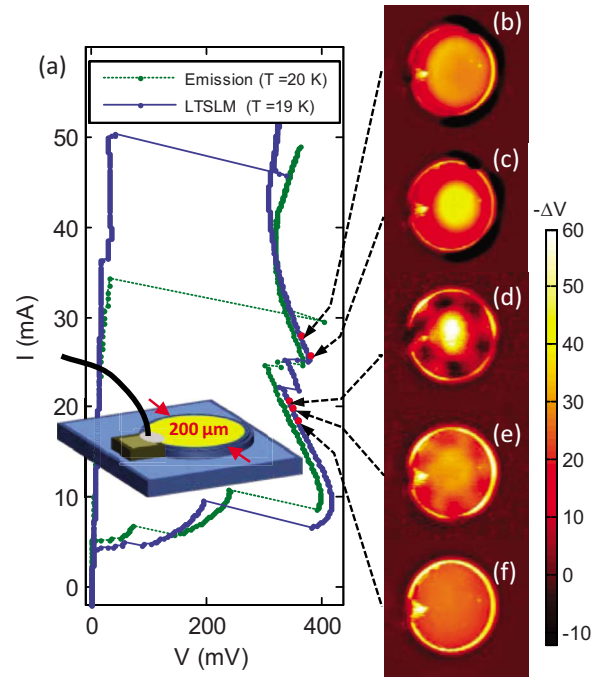


FIG. 3. (Color online) (a) IVCs, taken for LTSLM (blue dots connected by solid line) and for THz emission measurements (green dots connected by dotted line) and [(b)–(f)] LTSLM images of disk-shaped sample 1. Bias points where the images have been taken are indicated by arrows. Inset in (a) shows a sketch of the disk including the contacting lead.

images. Further, there is a strong edge signal arising because the mesas edges are not covered by gold; as a consequence, the laser-beam-induced temperature rise at the edge is larger than in the mesa interior. Apart from the signal caused by the wire and the edge effects, for currents below 19 mA the images are smooth, with $\Delta V < 0$. Figure 3(f) shows an example. At $I = 19.4$ mA a cartwheel-like pattern appears, having 6 “spokes,” cf. Fig. 3(e). In the center of the disk as well as on the spokes ΔV does not differ much to the case of Fig. 3(f). In between the spokes $|\Delta V|$ is lower than the background, i.e., a positive signal is added. At $I = 21$ mA, in addition to the cartwheel-like pattern a strong negative signal appears in the center of the disk, cf. Fig. 3(d). This signal grows with increasing bias current, cf. Figs. 3(c) and 3(b), and is indicative of a hot spot. As already mentioned, in LTSLM the *edge* of a hot spot produces the strongest response. Thus, the actual hot region in Fig. 3(d) is presumably still very small and the bright spot shows the transition region to the cold part of the mesa. In Fig. 3(c) $|\Delta V|$ still has maximum near the center of the disk while in Fig. 3(b) a dip appears near the center; the hot-spot signal becomes ring shaped.

The cartwheel-like pattern was visible for bias currents between 19 and 22 mA and is indicative of an $m=3, n=1$ cavity mode having six nodes in azimuthal direction. Here, $\chi_{mn}^c = 4.2$. In Fig. 4 we compare the measured patterns [Figs. 4(a) and 4(b)] to calculated cavity modes [Figs. 4(c) and 4(d)]. In Fig. 4(c) we have plotted the square of the amplitude of the electric field component, Fig. 4(d) shows the corresponding plot for the magnetic field. For the compari-

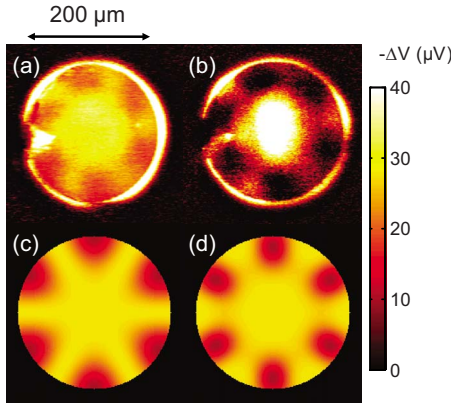


FIG. 4. (Color online) [(a) and (b)] LTSLM images, as measured at $I=19.4$ mA and $I=21$ mA, respectively, in comparison to the calculated distributions of the squares of (c) electric field and (d) magnetic field of the $m=3$, $n=1$ cavity mode. Color scale for the theoretical plots is made such that zeroes appear bright (yellow) and maxima appear dark (red).

son to the LTSLM data the color scale of the theoretical plots is chosen such that the zeroes of the standing waves appear in bright (yellow) color while the maxima are dark (red). For the magnetic field pattern, Fig. 4(d), one notes that the center region is hexagon shaped while the darkest regions are centered inside the disk. By contrast the electric field pattern, Fig. 4(c), is star shaped in the center of the disk while the maxima (dark regions) appear close to the outer perimeter. Figure 4(a) is an enlargement of Fig. 3(e), plotted on an enhanced color scale. The center part of the wave feature resembles the hexagon-shaped central structure of the magnetic field part of the cavity resonance. In Fig. 4(a) the dark regions seem to be located closer to the outer perimeter than in Fig. 4(d). However, the strong edge signal in LTSLM complicates the analysis of structures appearing close to the outer perimeter. Thus, we consider the structures appearing in the inner part of the disk more relevant and conclude that the magnetic field part of the cavity mode has been imaged in Fig. 4(a). In the LTSLM image Fig. 4(b), which is an enlargement of Fig. 3(d), the dark sections are more clearly located inside the disk and the hexagon structure is still visible in spite of the bright hot-spot feature. We thus conclude that also here the magnetic field has been imaged. Note that in the presence of a hot spot located in the center of the disk the superconducting part may be viewed as an *annular* mesa with an inner radius a_i corresponding to the hot-spot radius. The resonance mode imaged still corresponds to a $m=3$ mode. Since the $m=3$ mode has a zero in the center of the disk, for a small hot spot the standing-wave pattern visible in LTSLM outside the hot-spot region will not differ much from the case without hot spot. For a ring-shaped mesa the resonance frequencies are given by $c'\chi_{mn}/2\pi a$, where the coefficient χ_{mn} depends on the ratio a_i/a , cf. Eq. (15) in Ref. 41. Depending on n and m the resonance frequencies can either increase or decrease as a function of a_i/a . For the special case of a $m=3$, $n=1$ mode, χ_{31} is almost constant for $a_i/a < 0.3$; for $a_i/a=0.3$, $\chi_{31}=4.18$. For larger ratios of a_i/a , χ_{31} starts to decrease, having, e.g., a value of 3.75 for $a_i/a=0.6$. For the case of Fig. 3(d), $a_i/a \ll 1$, and thus $\chi_{mn} \approx \chi_{mn}^c$.

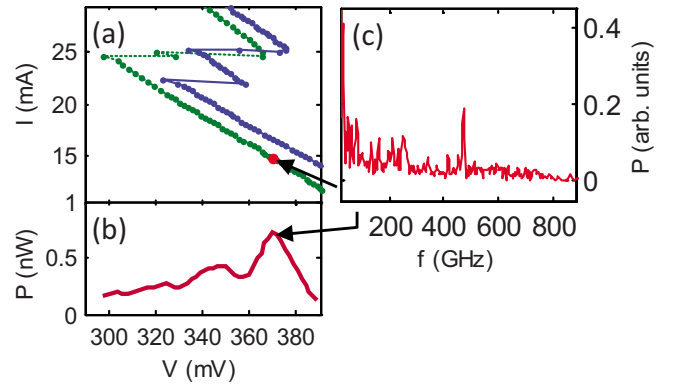


FIG. 5. (Color online) THz emission from sample 1: (a) enlargement of the IVC of Fig. 4(a) in the current and voltage range where emission has been detected; (b) detected emission power vs voltage across mesa; and (c) Fourier spectrum at a bias of 14.9 mA and 370 mV.

Next we analyze the THz emission detected from sample 1. Figure 5(a) shows an enlargement of the IVC of Fig. 3(a) for the current and voltage range where emission has been found (the same range where the cavity resonance was seen in LTSLM; note, however, that the IVCs measured in Tübingen and in Tsukuba slightly differ from each other, making it difficult to precisely assign LTSLM images and emission data. Emission peaks appear in the voltage range 330–380 mV, cf. Fig. 5(b), with a maximum *detected* power of about 0.8 nW. Extrapolated over 4π this yields a total power of order $0.25 \mu\text{W}$ which is actually almost an order of magnitude below the radiation power detected for rectangular stacks.^{24,32} Figure 5(c) shows a Fourier spectrum of this radiation, with the sample biased at 14.9 mA and 370 mV [corresponding to LTSLM image Fig. 3(e), where no hot spot has formed yet]. The radiation peak occurs at $f=472$ GHz. Using the Josephson relation, $f=N\dot{\Phi}_0$ with the flux quantum Φ_0 , we infer a junction number $N=380$, which corresponds to only about 60% of the 600 junctions contained in the mesa, as estimated from its $0.9 \mu\text{m}$ thickness. Thus, not all junctions participate in radiation. Finally, from the $m=3$, $n=1$ mode observed and from the emission frequency we find a mode velocity of $c' \approx 7 \times 10^7$ m/s, which is the value to be expected when the junctions oscillate in phase and the temperature is not too high.^{31,32} In Fig. 5(b) a second emission peak is visible at $V \approx 350$ mV. It might be attributed to the situation of Fig. 3(d) when the hot spot has nucleated and the cold part of the disk forms an annular structure. As discussed above, for a small hot-spot radius the cavity resonance frequency is almost the same as for the disk, assuming a constant mode velocity. On the other hand, with increasing temperature in the mesa, the mode velocity c' decreases^{31,32} and thus effectively lowers the resonance frequency, consistent with the observed double peak structure in Fig. 5(b). For bias currents $I > 25$ mA neither THz emission nor standing-wave patterns were detectable.

B. Hot-spot formation monitored by detector stacks

Sample 2 consists of a rectangular $330 \times 70 \mu\text{m}^2$ large and $0.5\text{-}\mu\text{m}$ -thick main mesa which is surrounded by small

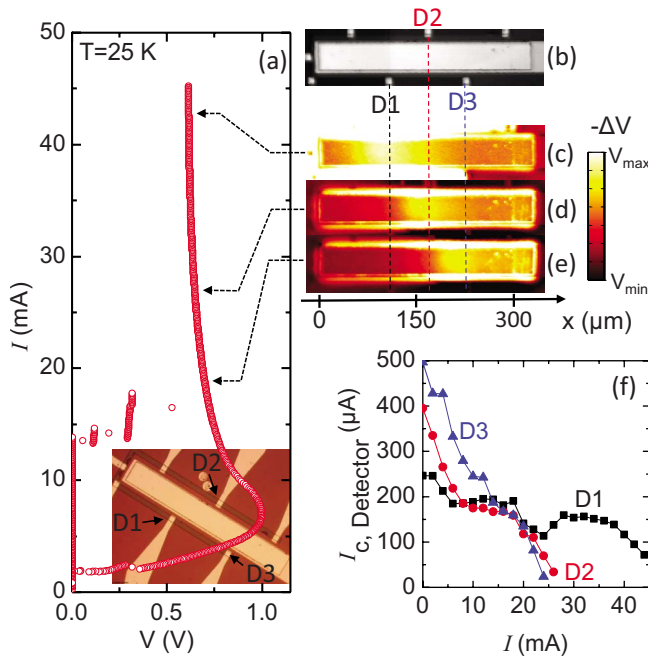


FIG. 6. (Color online) (a) IVC at $T=25$ K of sample 2 (main mesa) with optical image taken by the (b) laser microscope, [(c)–(e)] LTSLM images and (f) the critical current of detector junctions D1, D2, and D3 vs bias current through main mesa. Inset in (a) shows an optical image of sample 1, taken by a conventional microscope. Color bar for (c)–(e) denotes maximum and minimum values of $-\Delta V$. (c) $V_{\max}=100$ μ V, (d) 200 μ V, and (e) 320 μ V. $V_{\min}=-50$ μ V for all images.

mesas, cf. inset of Fig. 6(a). These mesas are separated by 10 μ m from the main mesa. Three of them (denoted D1, D2, and D3) worked. We suppose that the gold leads connecting the other detectors were broken during the fabrication process. An optical image, taken during LTSLM, of the main mesa and the surrounding detector mesas is shown in Fig. 6(b). The working detector mesas are indicated. The current I through the main mesa is injected from its right side. Originally the small mesas were intended to detect THz emission from the main mesa which, however, did not radiate. A possible reason is that the mesa was unusually thin (0.5 μ m). Still, the detectors were usable to estimate the temperature of the base crystal for different values of bias current through the main mesa. For this mesa, one observes a hot spot nucleating near the right end of the mesa; the hot-cold boundary forms a straight bright line moving to the left with increasing I . Figure 6(a) shows the IVC of the main mesa, measured at $T=25$ K. LTSLM image Fig. 6(e) is taken at $I=18.6$ mA. The right part of the mesa produces a negative response having a maximum near $x \approx 200$ μ m. Here, the edge of the hot spot is located. In Fig. 6(d), taken at $I=28.8$ mA, this maximum has moved to the left and is located near $x \approx 150$ μ m. Finally, in Fig. 6(c), taken at $I=42.4$ mA, the edge has moved to $x \approx 90$ μ m. In Fig. 6(c) there is also a strong response from *outside* the main mesa, roughly coinciding with the U-shaped mesa forming the base of the detector mesas [the dark structure in the inset of Fig. 6(a)]. We attribute this signal to parasitic IJJs shared by the main mesa and the U-shaped line. Such junctions are formed if, during ion mill-

ing, in the moat between the “U” and the main mesa less material has been removed than outside the U. A strong response ΔV can occur when the heating by the laser beam drives these junctions to their resistive state. Figure 6(f) shows the critical current I_c of the three detector junctions as a function of the current through the main mesa. As can be seen from Fig. 6(e), for $I=18.6$ mA the hot-spot edge, seen as the bright stripe inside the mesa, has just passed detector D3. I_c of this detector goes to zero at the not much higher current $I \approx 22$ mA, where I_c of detectors D1 and D2 are still finite. At $I=26.8$ mA the front of the hot spot has passed detector D2, cf. Fig. 6(d), consistent with the observation that I_c of this detector vanishes at $I \approx 25$ mA. Finally, I_c of detector D1 approaches zero near $I=45$ mA. For comparison, the front of the hot spot passes this detector for $I \approx 43$ mA, cf. Fig. 6(c). Exactly this behavior can be expected if, on one hand, the hot-spot feature observed indeed is a region heated to above T_c and, on the other hand the hot-spot region extends outside the main mesa. By contrast, the fact that I_c of a given detector falls to zero when being passed by the front of the hot spot is hard to understand if one assumes that the hot-spot region is below T_c and, e.g., corresponds to some nonequilibrium state with a suppressed superconducting gap. We thus conclude that our hot-spot interpretation is correct. For completeness we note that I_c of detector D1 has a minimum near $I=25$ mA. This feature is most likely an artifact caused by noise.

Still one should give some arguments how hot-spot formation occurs in the mesa geometry. The 3D heat flow equations have been solved numerically in Ref. 51, using COMSOL simulation software. The BSCCO crystal was assumed to be glued to a sapphire substrate, and a 100-nm-thick Au layer covering the mesa was assumed as the contacting electrode. The electrical and thermal properties of BSCCO and the various contacting layers were taken into account as close as possible. In the absence of heating, a linear IVC was assumed for the IJJs both above and below T_c . These calculations reproduced the appearance of a negative differential resistance region in the IVCs at high-bias case. With respect to the hot-spot formation they are in qualitative agreement with the LTSLM findings, although the temperature profile of the hot spot was roughly Gaussian shaped and thus relatively smooth. Further, the simulated hot spot appeared in the center of the mesa. In our experiments the hot spot often forms in the vicinity of the bias lead, although not at the attachment point itself. Qualitatively, this can be understood by considering a multiple role of this lead. First, it injects a current I into the upper layers of mesa. From here the current distributes both along and perpendicular to the CuO_2 layers. The interlayer current density will have a maximum in the vicinity of the lead, providing local heating in the resistive state. Additional local heating, growing quadratically with I , arises from the contact resistance between the bias lead and the mesa. By contrast, the lead also acts as a current-independent local heat sink. At low bias, Joule heating due to the applied current is not essential. With increasing bias Joule heating increases and will eventually lead to hot-spot formation near but not exactly at the lead.

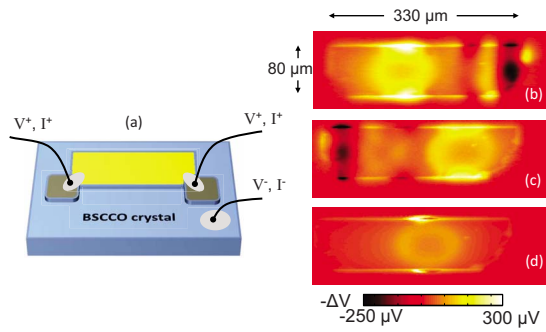


FIG. 7. (Color online) (a) Sketch of sample 3 and LTSLM data at $T=40$ K for various biasing conditions: (b) bias from left, (c) bias from right, and (d) symmetric bias. In the sketch, the yellow area symbolizes the Au layer covering the mesa. The dark squares at the lower mesa edges correspond to the insulating polyimide layer the gray dots symbolize the silver paste used to attach the contacting wires.

C. Manipulating hot spots and waves using two injection leads

In a number of experiments on rectangular mesas we observed that the hot spot often—although not always—nucleates near the current injection point. An obvious generalization is to use more than one current injection point. If the injection points are very far from each other one may simply expect the formation of several hot spots near the injection points. On the other hand, for not too large mesas a single hot spot might form at a position that depends on the ratio of injected currents. If so, the size of the cold part of the mesa and consequently wave formation should depend on the ratio of injected currents. Below we show data for two 330- μm -long rectangular mesas that were contacted at two opposite edges. We start with data obtained from a 80- μm -wide mesa (sample 3), cf. Fig. 7(a). In Figs. 7(b)–7(d) we show LTSLM images taken at $T=40$ K at a bias current of 30.4 mA. For image in Fig. 7(b) the current has been injected at the left contact. Here, the hot spot appears as a circular structure in the left half of the mesa and there is a clear standing-wave pattern in the right half of the stack. For the image in Fig. 7(c) the current has been injected from the right side. The hot spot now appears in the right half of the mesa and the wave is situated in the left part. Finally, Fig. 7(d) shows a symmetric situation where the current has been injected from both edges; half of the total current of 30.4 mA flows through each contact. Here, the hot spot is centered in the mesa and no wave appears. For these measurements we have varied the current injection points at fixed total bias current. The voltage across the sample, and thus the Josephson frequency, slightly changed for the three bias conditions, from 0.59 V when biasing from left, to 0.58 V when biasing from the right, and to 0.6 V for the symmetric bias. In the case of symmetric bias the injection leads were used both for voltage measurement and current injection; the resulting contact resistance is subtracted from the voltage quoted. To check whether this change in voltage is the dominant quantity for the (dis)appearance of the standing wave we have investigated hot-spot and wave formation for the symmetric bias

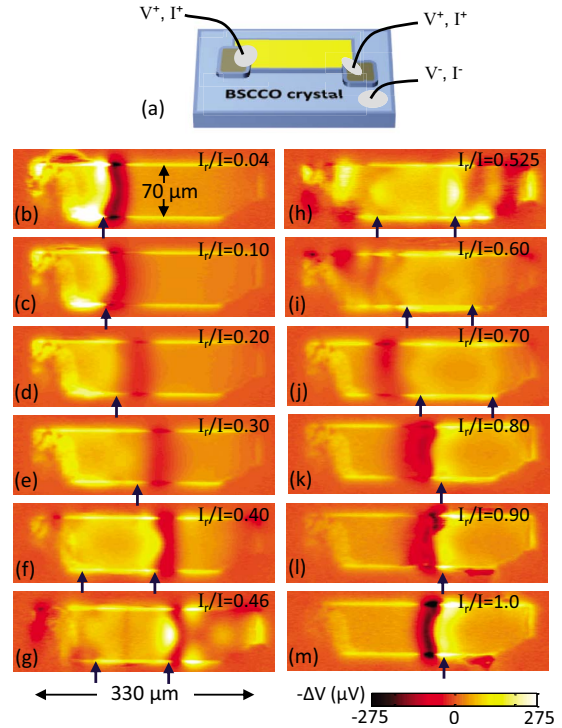


FIG. 8. (Color online) Sketch of sample 4, equipped with two current injectors (a) and (b) to (m) LTSLM data at $T=18$ K for various ratios of the current I_r through the right injector to the total current I . The ratios I_r/I are indicated in the graphs. Vertical arrows in LTSLM images indicate edges of hot spots.

and the bias-from-left configuration over a wide current range. As expected for a hot spot, its size increased with increasing input power. Regarding wave signals it turned out that, for the symmetric bias, we could not achieve a wave pattern at all. For the other configuration the wave appeared over a wide current range, from about 28–45 mA. Here, the voltage varied between 0.51 and 0.63 V, i.e., over a much larger range than for the case of Figs. 7(b)–7(d).

In Fig. 8 we show data for a 70- μm -wide mesa (sample 4). Accidentally, on the left edge the silver paste used to fix the current lead extends significantly into the mesa, as sketched in Fig. 8(a). On the right side the silver paste covers only the lower corner of the mesa. For this sample the asymmetry in the two bias currents was varied in small steps. Figures 8(b)–8(m) show LTSLM images at $T=18$ K. The total current was fixed at 38 mA. In the graphs the ratio I_r/I of the current through the right injector to the total current is indicated. For $I_r/I=0.04$ the hot spot is located on the left side of the mesa, see Fig. 8(b). In the graph, its edge is marked by an arrow. For $I_r/I=0.1$ the hot-spot position seems to be unchanged, see Fig. 8(c). By contrast, when increasing I_r/I toward symmetric bias, the hot-spot location moves toward the center of the mesa, see Figs. 8(d)–8(g). The shift seems to occur continuously. This also holds for ratios I_r/I between 0.5 and 0.9, as shown in Figs. 8(h)–8(l). No further change in the hot-spot position is visible between $I_r/I=0.9$ [Fig. 8(l)] and $I_r/I=1$ [Fig. 8(m)]. Note that, for I_r/I between 0.4 and 0.7 both the left and right edges of the hot spots are located inside the mesa, leaving two cold re-

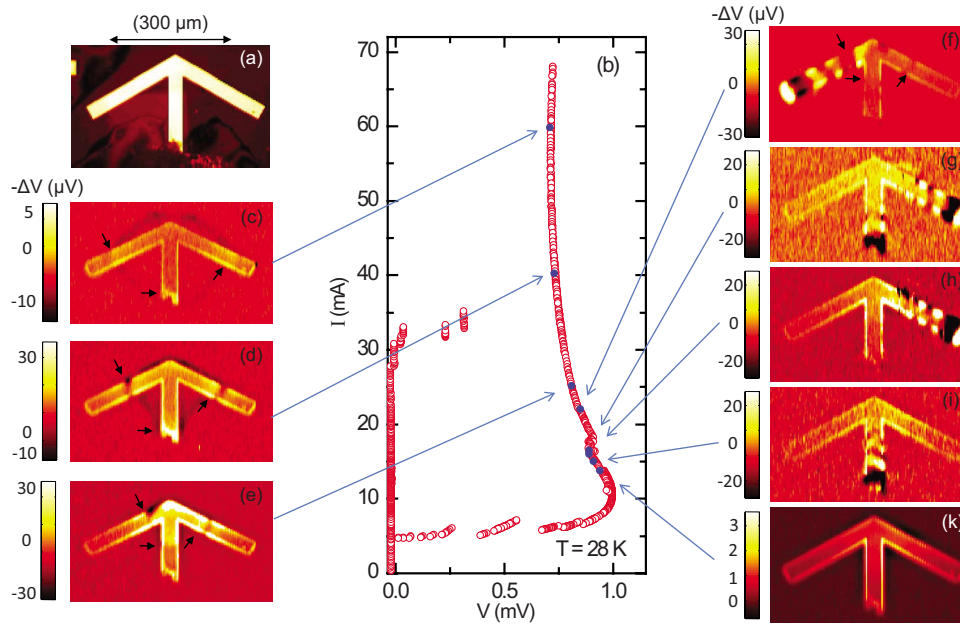


FIG. 9. (Color online) (a) Optical image, (b) current voltage characteristic, and [(c)–(k)] LTSLM images of the arrow-shaped sample 1, as measured at $T=28$ K. [(c)–(f)] Black arrows in images indicate edge of hot spot.

gions near the mesa edges. Further, in Fig. 8(g) a wavelike structure is visible in the right part of the mesa, although less clear as for sample 3 in Fig. 7(b). In Fig. 8(h) there seems to be an additional wave structure in the left part of the mesa which remains visible in Fig. 8(i) where the wave structure in the right part of the mesa has disappeared.

From our experiments on samples 3 and 4 we conclude that the hot-spot position can be varied more or less continuously by using different injection points. The experiments also support the picture that one of the roles of the hot spot simply is to adjust the size of the cavity, i.e., the cold part of the mesa. Thus, by using two or more injectors THz emission can be turned on and off in a more or less controlled way. We note, however, that for this purpose injectors should be patterned more reliably than just attaching wires by silver paste. This is feasible using standard lithographic techniques.

D. Hot-spot and wave formation in an arrow-shaped mesa

The last structure we discuss in this paper is an arrow-shaped mesa (sample 5), see Fig. 9(a). The structure, initially produced together with a “Y”-shaped mesa to study wave splitting at intersections, provides further insights into hot-spot nucleation points and wave formation.⁶³ The arrow was contacted on the foot of the arrow. The contact is visible in Fig. 9(a) and the LTSLM images, Figs. 9(c)–9(k). An IVC of the arrow, taken at a bath temperature of 28 K, is shown in Fig. 9(b). Starting from zero current the IJJs in the mesa switch to their resistive states at currents I between 30 and 35 mA. When lowering the current from high bias one observes an instability for currents between 18 and 16 mA that is indicative for the disappearance of a hot spot present at high bias. The LTSLM images are taken in the resistive state of all junctions. For currents decreasing from 60 to 25 mA one observes a diamond-shaped loop centered around the top of

the arrow but extending far out of the mesa. At $I=60$ mA, cf. Fig. 9(c), the loop is visible as a bright stripe *inside* each arm of the mesa, as indicated by arrows in Fig. 9(c). Outside the actual mesa structure the feature is continued by a positive (black) signal ΔV . At $I=40$ mA, cf. Fig. 9(d), the loop has decreased in diameter. On the tip of the arrow it appears close to the mesa edge while it still extends significantly beyond the mesa in between the three arms. At $I=25$ mA, cf. Fig. 9(e), the feature has reduced basically to the tip of the arrow. *Inside* the mesa the feature shows the same behavior that we typically see for the hot-spot boundary in narrow mesas, i.e., a stripe moving with growing input power. The fact that the structure visibly continues outside the mesa is, similar to the case of sample 2, understood best if one assumes that there are additional parasitic IJJs at the foot of the mesa, contributing to the voltage measured and acting as sensors for the hot/cold boundary of the hot spot. Independent of this explanation the data on one hand show that the hot spot extends beyond the actual mesa, in agreement with the data presented for sample 2. On the other hand, we see that the hot spot forms at the tip of the arrow rather than close to the current injection point.

When lowering the current, between 24 and 15 mA standing-wave patterns appear in various parts of the mesa. Near $I=22$ mA a wave pattern is visible in the left part of the arrow [Fig. 9(f)]. At $I=16.4$ mA a wave pattern appears in the right part of the arrow and the shaft [Fig. 9(g)], at $I=16.0$ mA the wave is visible only in the right part of the arrow [Fig. 9(h)] and at $I=15.0$ mA the wave appears only in the shaft [Fig. 9(i)]. For currents below 15 mA the LTSLM images were smooth and neither hot spot nor wave features appeared, see Fig. 9(k). Thus, in a narrow current range the arrow acted as a switch, generating standing waves in different arms of the structure. This property, which might be interesting for integrated layouts involving several mesa struc-

tures, can be understood if one assumes that a hot spot is located at the tip of the arrow. It separates the arrow effectively into three cavities which can become resonant or not, depending on the position of the hot-spot edges adjusting the size of the cavities. In Fig. 9(f) the diamond-shaped loop representing the hot spot is still vaguely visible. For Figs. 9(g)–9(i) we cannot tell. However, these images have been taken very close to the instability in the IVC (kink at 18 mA), making it likely that there is either still a small hot spot or at least a zone very close to T_c effectively separating the three cavities.

IV. CONCLUSIONS

In this paper we presented LTSLM and THz emission measurements on four different mesa geometries. These measurements improve the understanding of hot-spot and wave formation in intrinsic Josephson junction stacks. Concerning the standing waves the nontrivial geometry of a disk-shaped mesa, as opposed to rectangular structures studied previously, further confirmed the interpretation of the patterns observed as electromagnetic cavity modes. Despite the fact that most of the junctions were in the resistive state, the emitted power was almost one order of magnitude below the power emitted by the best rectangular structures studied. This may indicate that disk structures, although valuable for fundamental studies, are not superior to rectangular mesas with respect to THz oscillators. Concerning hot-spot formation, using a rectangular mesa with nearby detector mesas we found that the critical currents of the detectors vanished when being passed by the front of the hot spot. This is consistent with the hot-spot interpretation of the feature observed in LTSLM but would be hard to explain if the hot-spot region were still superconducting and corresponds to, e.g., a region of suppressed superconducting gap. Our intention with the two other geometries—a rectangular mesa equipped with two current injectors and an arrow-shaped structure—was to check whether the hot spot and the wave formation could be controlled. Using two current injectors we have realized, for constant total bias current, different hot-spot locations depending on the ratio of currents through the two injectors. For certain hot-spot positions waves appeared in either the left or the right part of the mesa. In the arrow-shaped structure-independent wave formation was observed in the three parts of the arrow, that were presumably separated and changed in size by a hot spot located at the tip of the arrow. While often the hot spot nucleates near the current injection point, this geometry also showed that nucle-

ation centers can have different (geometric) origin, i.e., the tip of the arrow in the present case.

These results point out ways to control hot-spot and THz wave formation in the high-bias regime. However, the reproducibility of the device properties needs further improvement. For example, not all samples radiate and, for the radiating samples, we cannot precisely predict the emission frequency range. The hot-spot formation results from a delicate balance between the dissipated power and heat flowing (or escaping) through the electrical leads and various thin-film layers involved. Thus, the precise thermal properties differ not only for different mesas but even depend on the setup. In addition, suitable models of hot-spot nucleation, THz generation and the interaction between hot spots and wave are lacking. Our results may have shown that one of the roles of the hot spot is to form an adjustable end of the cavity formed by the cold part of the mesa. In LTSLM the width of the hot/cold transition region typically has a width of 20–30 μm . This width, which may be resolution limited, is well below the typical wavelengths of the cavity modes excited (around 100 μm). Thus, changes in conductance between the hot and cold parts seem to be abrupt enough to lead to electromagnetic wave reflection at the hot-spot edge. One can further assume that, in the presence of a standing wave, the cold part of the mesa experiences additional heating at the positions of the wave antinodes, contributing to the heat balance of the whole mesa. This should cause backaction to the hot-spot position and may lead to some extent to a “self-alignment” of the hot-spot position relative to the wave. There may be additional interactions between the hot spot and the THz waves. For example, the hot part of the mesa could act as an external shunt, helping in synchronizing the junctions in the stack. Also, nonequilibrium processes at the hot-spot edge may contribute to synchronization. Some discussion in the context of the linewidth of the terahertz emission observed is given in Ref. 32. Solving at least some of these issues is the task for the near future.

ACKNOWLEDGMENTS

We thank A. Yurgens, V. M. Krasnov, U. Welp, L. Ozyuzer, K. Kadowaki, I. Iguchi, K. Nakajima, and C. Otani for valuable discussions. Financial support by the strategic Japanese-German International Cooperative Program of the JST and the DFG, by the German Israeli Foundation via research under Grant No. G-967-126.14/2007, and by Grants-in-Aid for scientific research from JSPS is gratefully acknowledged.

*wang.huabing@nims.go.jp

†kleiner@uni-tuebingen.de

¹V. P. Koshelets and S. Shitov, *Supercond. Sci. Technol.* **13**, R53 (2000).

²P. A. A. Booi and S. P. Benz, *Appl. Phys. Lett.* **68**, 3799 (1996).

³P. Barbara, A. B. Cawthorne, S. V. Shitov, and C. J. Lobb, *Phys.*

Rev. Lett. **82**, 1963 (1999).

⁴M. Darula, T. Doderer, and S. Beuven, *Supercond. Sci. Technol.* **12**, R1 (1999).

⁵X. Hu and S. Z. Lin, *Supercond. Sci. Technol.* **23**, 053001 (2010).

⁶F. Song, F. Müller, R. Behr, and M. Klushin, *Appl. Phys. Lett.*

- 95**, 172501 (2009).
- ⁷I. Ottaviani, M. Cirillo, M. Lucci, V. Merlo, M. Salvato, M. G. Castellano, G. Torrioli, F. Mueller, and T. Weimann, *Phys. Rev. B* **80**, 174518 (2009).
- ⁸R. Kleiner, F. Steinmeyer, G. Kunkel, and P. Müller, *Phys. Rev. Lett.* **68**, 2394 (1992).
- ⁹R. Kleiner and P. Müller, *Phys. Rev. B* **49**, 1327 (1994).
- ¹⁰A. A. Yurgens, *Supercond. Sci. Technol.* **13**, R85 (2000).
- ¹¹R. Kleiner, *Phys. Rev. B* **50**, 6919 (1994).
- ¹²G. Hechtfisher, R. Kleiner, A. V. Ustinov, and P. Müller, *Phys. Rev. Lett.* **79**, 1365 (1997).
- ¹³G. Hechtfisher, W. Walkenhorst, G. Kunkel, K. Schlenga, R. Kleiner, P. Müller, and H. L. Johnson, *IEEE Trans. Appl. Supercond.* **7**, 2723 (1997).
- ¹⁴K. Lee, W. Wang, I. Iguchi, M. Tachiki, K. Hirata, and T. Mochiku, *Phys. Rev. B* **61**, 3616 (2000).
- ¹⁵M. Machida, T. Koyama, A. Tanaka, and M. Tachiki, *Physica C* **330**, 85 (2000).
- ¹⁶T. Clauss, T. Ushida, M. Mößle, D. Koelle, and R. Kleiner, *Appl. Phys. Lett.* **85**, 3166 (2004).
- ¹⁷S. Madsen, G. Filatella, and N. F. Pedersen, *Eur. Phys. J. B* **40**, 209 (2004).
- ¹⁸H. B. Wang, S. Urayama, S. M. Kim, S. Arisawa, T. Hatano, and B. Y. Zhu, *Appl. Phys. Lett.* **89**, 252506 (2006).
- ¹⁹V. M. Krasnov, *Phys. Rev. Lett.* **97**, 257003 (2006).
- ²⁰I. Batov, X. Jin, S. Shitov, Y. Koval, P. Müller, and A. Ustinov, *Appl. Phys. Lett.* **88**, 262504 (2006).
- ²¹A. Grib, M. Mans, J. Scherbel, M. Büenefeld, F. Schmidl, and P. Seidel, *Supercond. Sci. Technol.* **19**, S200 (2006).
- ²²M. H. Bae, H.-J. Lee, and J.-H. Choi, *Phys. Rev. Lett.* **98**, 027002 (2007).
- ²³S. O. Katterwe and V. M. Krasnov, *Phys. Rev. B* **80**, 020502 (2009).
- ²⁴L. Ozyuzer *et al.*, *Science* **318**, 1291 (2007).
- ²⁵K. Kadowaki *et al.*, *Physica C* **468**, 634 (2008).
- ²⁶L. Ozyuzer *et al.*, *Supercond. Sci. Technol.* **22**, 114009 (2009).
- ²⁷H. Minami, I. Kakeya, H. Yamaguchi, T. Yamamoto, and K. Kadowaki, *Appl. Phys. Lett.* **95**, 232511 (2009).
- ²⁸K. Kadowaki, M. Tsujimoto, K. Yamaki, T. Yamamoto, T. Kashiwagi, H. Minami, M. Tachiki, and R. A. Klemm, *J. Phys. Soc. Jpn.* **79**, 023703 (2010).
- ²⁹C. Kurter *et al.*, *IEEE Trans. Appl. Supercond.* **19**, 428 (2009).
- ³⁰K. E. Gray, L. Ozyuzer, A. E. Koshelev, C. Kurter, C. Kadowaki, T. Yamamoto, H. Minami, H. Yamaguchi, M. Tachiki, W.-K. Kwok, and U. Welp, *IEEE Trans. Appl. Supercond.* **19**, 886 (2009).
- ³¹H. B. Wang, S. Guénon, J. Yuan, A. Iishi, S. Arisawa, T. Hatano, T. Yamashita, D. Koelle, and R. Kleiner, *Phys. Rev. Lett.* **102**, 017006 (2009).
- ³²H. B. Wang *et al.*, *Phys. Rev. Lett.* **105**, 057002 (2010).
- ³³H. Minami, N. Orita, T. Koike, T. Yamamoto, and K. Kadowaki, *Physica C* (to be published).
- ³⁴N. Orita, H. Minami, T. Koike, T. Yamamoto, and K. Kadowaki, *Physica C* (to be published).
- ³⁵M. Tsujimoto, K. Yamaki, K. Deguchi, T. Yamamoto, T. Kashiwagi, H. Minami, M. Tachiki, K. Kadowaki, and R. A. Klemm, *Phys. Rev. Lett.* **105**, 037005 (2010).
- ³⁶K. Yamaki, M. Tsujimoto, T. Yamamoto, H. Minami, and K. Kadowaki, *Physica C* (to be published).
- ³⁷L. N. Bulaevskii and A. E. Koshelev, *Phys. Rev. Lett.* **99**, 057002 (2007).
- ³⁸A. E. Koshelev and L. N. Bulaevskii, *Phys. Rev. B* **77**, 014530 (2008).
- ³⁹A. E. Koshelev, *Phys. Rev. B* **78**, 174509 (2008).
- ⁴⁰S. Lin and X. Hu, *Phys. Rev. Lett.* **100**, 247006 (2008).
- ⁴¹X. Hu and S. Z. Lin, *Phys. Rev. B* **80**, 064516 (2009).
- ⁴²R. A. Klemm and K. Kadowaki, *J. Phys.: Condens. Matter* **22**, 375701 (2010).
- ⁴³Y. Nonomura, *Phys. Rev. B* **80**, 140506 (2009).
- ⁴⁴M. Tachiki, S. Fukuya, and T. Koyama, *Phys. Rev. Lett.* **102**, 127002 (2009).
- ⁴⁵T. Koyama, H. Matsumoto, M. Machida, and K. Kadowaki, *Phys. Rev. B* **79**, 104522 (2009).
- ⁴⁶N. Pedersen and S. Madsen, *IEEE Trans. Appl. Supercond.* **19**, 726 (2009).
- ⁴⁷V. M. Krasnov, *Phys. Rev. Lett.* **103**, 227002 (2009).
- ⁴⁸A. Grib and P. Seidel, *Phys. Status Solidi (RRL)* **3**, 302 (2009).
- ⁴⁹S. Savel'ev, V. A. Yampol'skii, A. L. Rakhmanov, and F. Nori, *Rep. Prog. Phys.* **73**, 026501 (2010).
- ⁵⁰H. Matsumoto, T. Koyama, and M. Machida, *Physica C* **470**, 1485 (2010).
- ⁵¹A. A. Yurgens [arXiv:1005.2932v1](https://arxiv.org/abs/1005.2932v1) (unpublished).
- ⁵²M. Tachiki, K. Ivanovic, K. Kadowaki, and T. Koyama, (unpublished).
- ⁵³W. J. Skocpol, M. R. Beasley, and M. Tinkham, *J. Appl. Phys.* **45**, 4054 (1974).
- ⁵⁴A. V. Gurevich and R. G. Mints, *Rev. Mod. Phys.* **59**, 941 (1987).
- ⁵⁵R. C. Dynes, V. Narayanamurti, and J. P. Garno, *Phys. Rev. Lett.* **39**, 229 (1977).
- ⁵⁶K. E. Gray and H. W. Willemsen, *J. Low Temp. Phys.* **31**, 911 (1978).
- ⁵⁷I. Iguchi and D. N. Langenberg, *Phys. Rev. Lett.* **44**, 486 (1980).
- ⁵⁸H. Akoh and K. Kajimura, *Phys. Rev. B* **25**, 4467 (1982).
- ⁵⁹R. Gross, D. B. Schmid, and R. P. Huebener, *J. Low Temp. Phys.* **62**, 245 (1986).
- ⁶⁰S. G. Lachenmann, T. Doderer, R. P. Huebener, D. Quenter, J. Niemeyer, and R. Pöpel, *Phys. Rev. B* **48**, 3295 (1993).
- ⁶¹R. Eichele, L. Freytag, H. Seifert, R. P. Huebener, and J. R. Clem, *J. Low Temp. Phys.* **52**, 449 (1983).
- ⁶²H. Eisele, M. Naftaly, and J. Fletcher, *Meas. Sci. Technol.* **18**, 2623 (2007).
- ⁶³Similar to the arrow also the Y was contacted at its lower edge. The assumption was that the hot spot will nucleate near this contact; if the waves originate from the hot-spot edge, both structures would have allowed to study if and how the wave splits at the intersections. In experiment the Y did not work. For the arrow structure the hot spot formed at the tip of the arrow, producing the results discussed in the text.